Journal of Alloys and Compounds, 206 (1994) 83–93
JALCOM 1012

Deuterium absorption and material phase characteristics of Zr_2Fe

A. Nobile
Engineering Sciences and Applications Division, Los Alamos National Laboratory, Los Alamos, NM 87545 (USA)

W.C. Mosley, J.S. Holder and K.N. Brooks
Westinghouse Savannah River Co., Savannah River Technology Center, Savannah River Site, Aiken, SC 29808 (USA)

(Received June 29, 1993; in final form September 29, 1993)

Abstract

Deuterium absorption and material phase characteristics of Zr_2Fe (SAES St 198) were studied. Scanning electron microscope images of polished surfaces, electron probe microanalysis and X-ray powder diffractometry indicated the presence of a continuous Zr_2Fe phase with secondary phases of $ZrFe_2$, Zr_5FeSn, α-Zr and Zr_6Fe_3O. A statistically-designed experiment to determine the effects of temperature, time and vacuum quality on activation of St 198 revealed that when activated at low temperature (350 °C) deuterium absorption rate at 350 °C was slower when the vacuum quality was poor (2.5 Pa *vs.* 3×10^{-4} Pa). However, at higher activation temperature (500 °C), deuterium absorption rate at 350 °C was fast and was independent of vacuum quality. Deuterium pressure–composition–temperature (*P–C–T*) data are reported for St 198 in the temperature range 200–500 °C. The *P–C–T* data over the full range of deuterium loading and at temperatures of 350 °C and below are described by the following expression given in terms of the equilibrium D_2 absorption pressure, P_{D_2}, and the getter loading, q:

$$K_0 e^{-(\Delta H_a/RT)} = \frac{q^2}{P_{D_2}(q^*-q)^2}$$

where ΔH_a and K_0 have values of 101.8 kJ mol^{-1} and 3.24×10^{-8} Pa^{-1}, respectively, and q^* is 15.998 kPa L^{-1} g^{-1}. At higher temperatures, one or more secondary reactions in the solid phase occur that slowly consume D_2 from the gas phase. X-ray diffraction and other data suggest these reactions to be:

$$2Zr_2FeD_x \longrightarrow xZrD_2 + \frac{x}{3}ZrFe_2 + \left(2-\frac{2}{3}x\right)Zr_2Fe$$

$$Zr_2FeD_x + \left(2-\frac{1}{2}x\right)D_2 \longrightarrow 2ZrD_2 + Fe$$

where $0<x<3$. Reaction between gas phase deuterium and Zr_2Fe formed in the first reaction accounts for the observed consumption of deuterium from the gas phase by this reaction.

1. Introduction

A metal getter having the nominal composition Zr_2Fe, that is produced and sold by SAES Getters under the trade name St 198, has the unique property of being reactive with hydrogen isotopes, oxygen, water and other gases, while remaining relatively unreactive toward nitrogen. Further, the material is available in the form of pressed pellets that can be used in packed bed reactors with minimal gas pressure drop. These properties allow this getter to be considered a candidate for tritium removal from nitrogen glovebox atmospheres and inert gas process streams having low tritium concentrations. Removal of tritium from glovebox atmospheres with metal getters has the advantage of avoiding formation of highly radiotoxic tritiated water, as is the case with conventional glovebox tritium removal systems that canalytically oxidize tritium to water and trap tritiated water on molecular sieves.

Kherani *et al.* [1] studied tritium removal from flowing nitrogen using an SAES St 198/700 purifier cartridge. Tritium in nitrogen with initial concentrations less than 1 mCi m^{-3} was removed to levels undetectable by their ion chamber. However, for initial concentrations higher than 1 mCi m^{-3}, tritium breakthrough was observed, and it was further shown that the amount of breakthrough increased with flow rate and initial tritium concentration. A glovebox tritium cleanup system based

Elsevier Sequoia
SSDI 0925-8388(93)01012-S

on the use of St 198 has been designed and built by the Ontario Hydro Research Division [2], and in fact, in a collaborative effort between SAES Getters and Ontario Hydro Research, a tritium cleanup system using St 198 has been designed for commercial sale. Tritium tests with the Ontario Hydro Research glovebox unit demonstrated successful removal of tritium from the glovebox atmosphere. However, tritium breakthrough behavior at higher tritium concentrations, similar to that observed by Kherani *et al.*, was seen.

The above work has demonstrated the usefulness of St 198 for tritium cleanup systems. It is likely that improvements to the getter bed design will eliminate tritium breakthrough at higher concentrations and flow rates. Programs are underway at three US tritium laboratories to develop technology that uses metal getters for removing tritium from glovebox and process atmospheres. Previous experiments in developing metal hydride tritium handling processes [3] has demonstrated that a thorough understanding of hydrogen isotope absorption properties and material phase characteristics of metal hydride forming materials is essential for a number of reasons. This paper reports results from a study to characterize the deuterium pressure–composition–temperature (*P–C–T*) behavior, as well as the material phase characteristics of St 198. Other aspects such as activation of the getter and undesirable secondary reactions that occur in the Zr_2Fe lattice at high temperature while loaded with deuterium were also investigated. Additionally, we report a number of physical parameters, such as densities and pore structure data that are useful for metal getter reactor design calculations.

Some data on the hydrogen absorption behavior of Zr_2Fe exists in the literature. Manini *et al.* [4] and Boffito *et al.* [5] provide hydrogen absorption isotherms for St 198 at temperatures between 200 and 700 °C. Both of these publications provide correlations that relate the hydrogen absorption pressure to temperature and getter hydrogen content. While the material has a total hydrogen capacity approaching 16 kPa L g^{-1}, the correlation of Manini *et al.* applies to hydrogen loadings less than 1.5 kPa L g^{-1}, and the correlation reported by Boffito *et al.* applies to hydrogen loadings less than 0.66 kPa L g^{-1}. Manini *et al.* [4] also report that at temperatures higher than 500 °C, hydrogen never reached equilibrium with the material, apparently due to a slow reaction of Zr_2FeH_x to ZrH_2 and $ZrFe_2$. These workers further show that at low hydrogen loading only partial conversion of Zr_2FeH_x to ZrH_2 and $ZrFe_2$ occurs, but at high loadings complete conversion to ZrH_2 and $ZrFe_2$ occurs. Their samples were held at 500 °C for 2 h. Van Essen and Buschow [6], who investigated hydrogen absorption in several Zr- and Hf-based intermetallic compounds, state that hydrogen uptake in Zr_2Fe does not form a stable hydride, but decomposes to $ZrFe_2$ and ZrH_2 when activated for 4 h at 50 °C and under 4.05 MPa of hydrogen pressure. Decomposition of hydrogen-loaded Zr_2Fe to $ZrFe_2$ and ZrH_2 was later confirmed by Aubertin and coworkers [7], who exposed Zr_2Fe at 850 °C to 100 kPa of hydrogen for 15 h.

2. Experimental details

2.1. Elemental analysis

St 198 getter in the form of 4 mm long×6 mm diameter pressed pellets was purchased from SAES Getters, Colorado Springs, Colorado. Solutions obtained by acid dissolution of the getter were analyzed by inductively coupled plasma–mass spectrometry (ICP–MS) to determine the getter elemental composition. Dissolution of the getter was accomplished by addition of 0.1 g sample to 8 ml aqua regia, followed by overnight heating at 95 °C. The remaining residue was then dissolved by adding 2 ml of HF. This solution was then diluted for analysis by ICP–MS. Getter material was also analyzed by X-ray fluorescence (XRF) without standards, but this method is qualitative, and is not expected to be as accurate as ICP–MS.

2.2. Pellet physical properties

The pore structure of St 198 pellets was characterized with a Micromeritics Auto-Pore II Model 9220 mercury intrusion porosimeter. A number of parameters such as pellet void fractions and pellet densities of the as-received pellets were measured. Packed bed void fractions were measured for two different pellet sizes.

2.3. Material phase characteristics

Scanning electron microscopy (SEM) was used to obtain images of polished surfaces on St 198 pellets in order to visually examine the phases present in the material. Energy dispersive X-ray analysis yielded qualitative elemental analyses of selected areas on the particle surface. Quantitative analyses of selected areas were obtained by electron probe microanalysis (EPMA). X-ray intensities were compared with zirconium, iron and tin standards using corrections for atomic number, absorption and fluorescence (ZAF corrections). X-ray diffractometry (XRD) was performed on powder obtained from crushing St 198 pellets. Copper Kα radiation was used to scan the 2θ range from 5 to 135°. Phases were identified by matching crystallographic diffraction peak interplanar spacings (d-values) and relative intensities with reference XRD data [8].

2.4. Activation study

The St 198 getter was activated by holding samples under vacuum at temperatures above about 350 °C for several hours. During activation, a highly reactive metal surface is produced by oxygen diffusion into the bulk [9–11], or by cracking of the surface oxide layer. To determine the optimum activation conditions, the effects of temperature, time and vacuum quality on activation of the material were investigated by performing a 2^3 factorial experiment. Samples were activated at temperatures of 350 and 500 °C, for periods of 4 and 16 h, and under evacuation by a Welch Duo-Seal two stage rotary vane pump (2.5 Pa) or an Alcatel Drytel 30 fluidless vacuum pump (3×10^{-4} Pa). A cold trap was not used with either pump. The extent of activation was determined by measuring the initial deuterium absorption rate at 350 °C. High initial deuterium absorption rate is indicative of a well-activated sample. Absorption rate measurements were performed on the gas manifold shown schematically in Fig. 1(a). Samples (*ca.* 1 g) were held in the sample cell shown in Fig. 1(b), which was wrapped with electrical heating tape. A temperature controller kept the sample temperature constant within 1 °C. After activation of the sample, a data acquisition computer recorded pressure *vs.* time data after opening a valve between the sample and a 300 ml calibrated volume that contained 4000 Pa (30 T) deuterium. Pressure was measured with an MKS Baratron 390H 0–133 kPa capacitance manometer.

2.5. P–C–T measurements

Deuterium *P–C–T* behavior for St 198 samples was investigated using the same gas manifold, sample cell, and sample size described above. Absorption isotherms were measured at temperatures in the range 200–500 °C. Prior to each isotherm measurement, a fresh sample was loaded into the sample cell and activated by evacuating with an Alcatel Drytel 30 vacuum pump to $<3\times10^{-4}$ Pa at 350 °C for 4 h. Static absorption isotherm measurements were automated with a data acquisition computer. After admitting an aliquot of gas to the sample, the sample was allowed to equilibrate for 20 min. A 0–1.33 kPa MKS Baratron 390H capacitance manometer was used to measure the pressure in equilibrium with the samples.

3. Results

3.1. Elemental analysis

Results from ICP–MS and XRF elemental analyses of St 198 are shown in Table 1. Boffito *et al.* [5] reported St 198 to have the composition 76.5 wt.% Zr, 23.5 wt.% Fe. Our iron analysis agrees closely with that of Boffito *et al.*, but we detect slightly less zirconium, and the presence of some tin (1.2%). Zn, Cu, Ti, La and Cr are most likely impurities, and probably do not influence the getter behavior significantly. As will be shown below, tin plays a significant role in the phase behavior of the material. XRF analysis is only qualitative, and does not agree with ICP–MS. However, XRF shows the presence of copper, which was not detected by ICP–MS.

3.2. Pellet physical properties

St 198 pellets are formed by compacting irregular alloy granules with maximum dimensions of about 150 μm, as shown in Fig. 2. Pore size distribution data for St 198 pellets expressed as incremental intrusion volume *vs.* diameter are shown in Fig. 3. The majority of the pores are in the 2–5 μm diameter range, with most of the remaining pores being in the 0.2–2 μm range. The material has very few pores with diameters less than 0.1 μm. Each 6 mm diameter ×4 mm long St 198 pellet weighed 0.6 g, corresponding to a pellet density of 5.3 g cm^{-3}, which is in close agreement with the

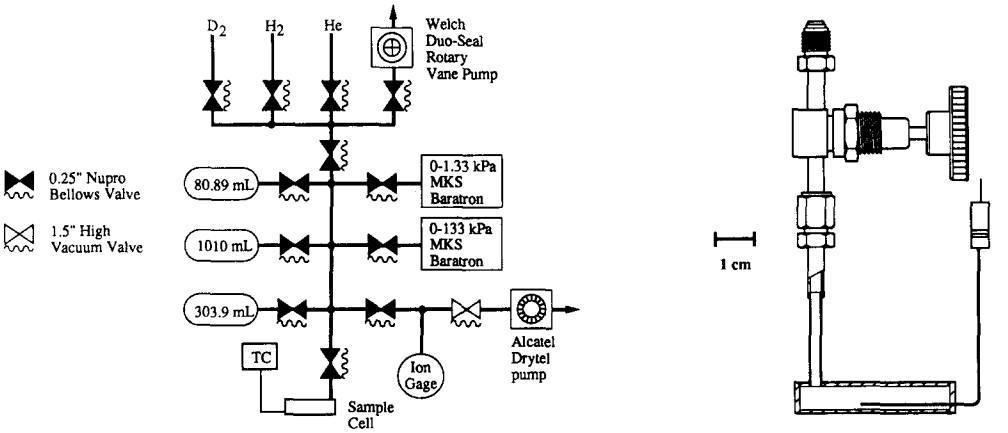

Fig. 1. (a) Schematic arrangement of the apparatus used for activation and *P–C–T* studies on St 198 samples, (b) sample cell.

TABLE 1. Elemental analysis of as-received SAES St 198 by inductively coupled plasma mass spectrometry (ICP–MS) and X-ray fluorescence (XRF)

Element	Weight percent	
	ICP–MS	XRF
Zr	73.6	81.8
Fe	23.3	16.9
Sn	1.2	1.0
Zn	0.5	–
Cu	–	0.3
Ti	0.1	–
La	0.07	–
Cr	0.06	–

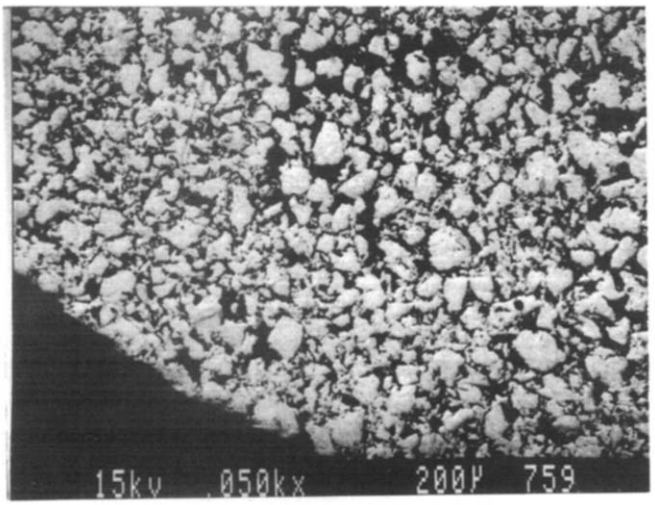

Fig. 2. SEM image of an as-received SAES St 198 pellet surface.

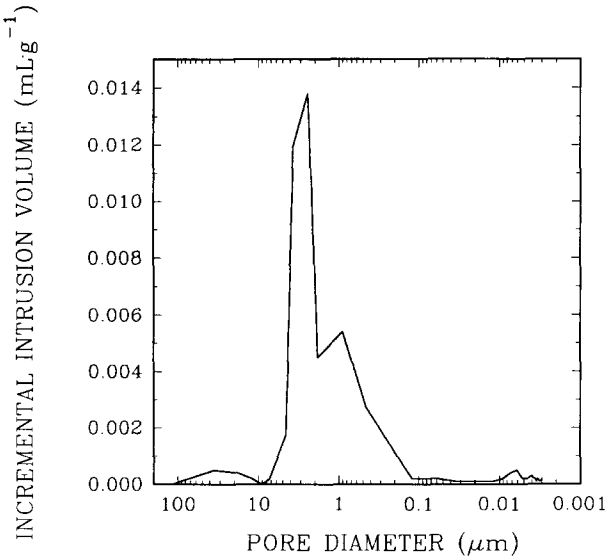

Fig. 3. Incremental intrusion volume *vs.* pore diameter for as-received SAES St 198 pellets.

TABLE 2. Summary of as-received SAES St 198 pellet physical characterization parameters

Property	Value
Total intrusion volume	0.0479 ml g^{-1}
Total pore area	2.523 m^2 g^{-1}
Median pore diameter (vol)	2.8443 μm
Median pore diameter (area)	0.0042 μm
Average pore diameter ($4V/A$)	0.0759 μm
Pellet density	5.1689 g ml^{-1}
Theoretical density	6.8697 g ml^{-1}
Pellet void fraction	0.25
Packed bed void fraction (4 mm×6 mm pellets)	0.43

value of 5.17 measured by porosimetry. The theoretical density of 6.8697 g cm^{-3} measured by porosimetry agrees well with the value of 6.938 g cm^{-3} obtained from X-ray powder diffraction files [8].

The void fraction of 0.25 calculated from the pellet and theoretical densities in Table 2 is slightly lower than the value of 0.31 that we determined from gas expansion measurements. The higher value obtained by gas expansion suggests the presence of small pores not accessible by the mercury intrusion method. However, the close agreement between theoretical densities obtained from the powder diffraction files and porosimetry is inconsistent with inaccessible porosity in the sample, so it is more likely that the deviation is attributable to the larger error associated with the gas expansion technique. Thus, the value from the porosimetry measurements is probably more reliable.

The tap density of a packed bed of 4 mm long ×6 mm diameter pellets was measured to be 2.93 g ml^{-1}. From this, a void fraction of 0.43 for the bed is calculated, and represents the void fraction associated with volume between individual pellets in the bed.

3.3. Material phase characteristics

Figure 4 shows an SEM backscattered electron (BSE) image of the polished surface of an St 198 pressed pellet. Phases darker in intensity are of lower atomic number. The primary (continuous) phase of medium density has been determined by EPMA to have the composition $Zr_{0.660\pm0.018}Fe_{0.337\pm0.019}Sn_{0.003\pm0.001}$, that corresponds to Zr_2Fe. The dark secondary phase had the composition $Zr_{0.350\pm0.01}Fe_{0.650\pm0.010}$ that corresponds to $ZrFe_2$. Inclusions of a bright secondary phase, consisting mostly of micrometer-wide stringers within the primary phase in regions of eutectic, contained tin in addition to iron and zirconium. EPMA was not able to resolve the small bright inclusions in eutectic regions. Analysis of eutectic areas yielded compositions of 73.3±1.6 at.% (a/o) zirconium, 25.5±1.6 a/o iron, and 1.2±0.6 a/o tin. However, three points in the

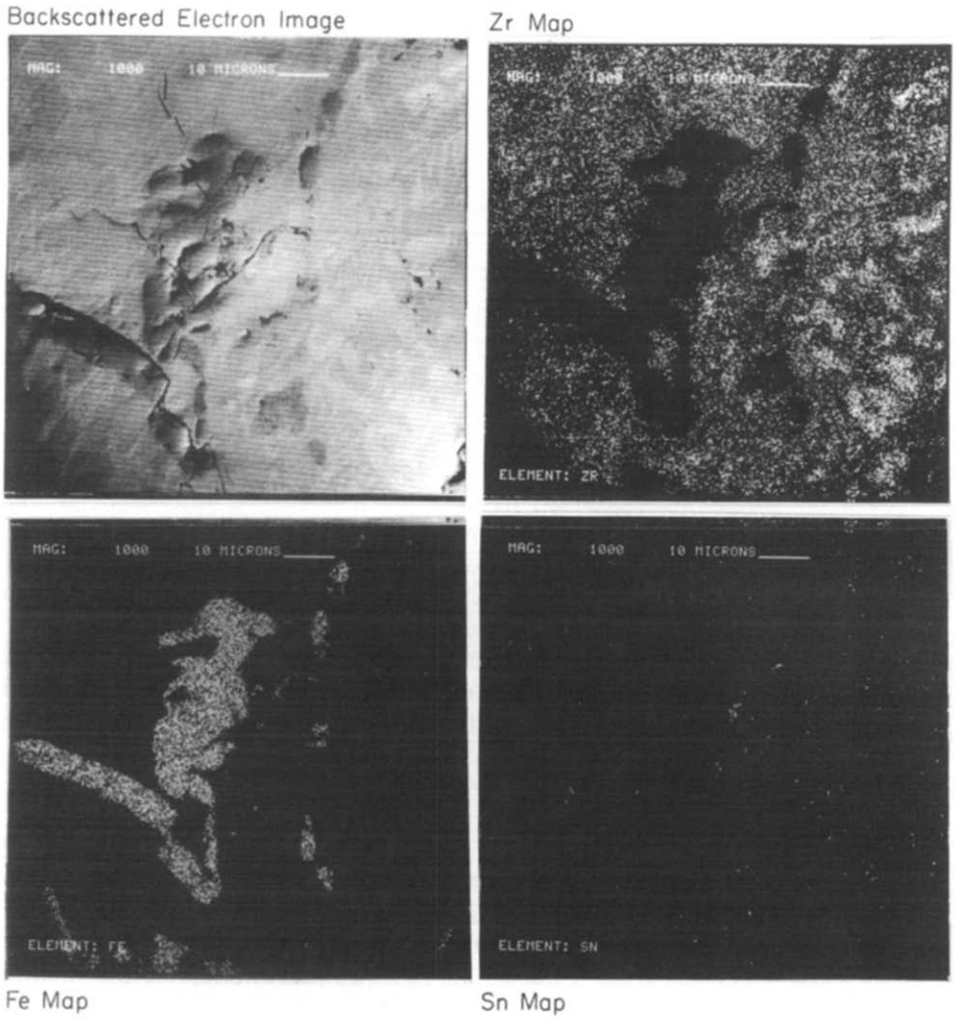

Fig. 4. SEM BSE image and elemental maps of the polished surface of an as-received St 198 pellet.

bright secondary phase yielded $Zr_{0.715\pm0.01}Fe_{0.15\pm0.019}Sn_{0.314\pm0.026}$, which corresponds to Zr_5FeSn. Two zirconium-rich points of compositions 79 a/o Zr, 17.7 a/o Fe, 3.3 a/o Sn and 82.8 a/o Zr, 13.0 a/o Fe, 4.3 a/o Sn were also detected.

An XRD pattern for as-received St 198 indicated the presence of the four phases Zr_2Fe, $ZrFe_2$, α-Zr and Zr_6Fe_3O [8]. Although Zr_6Fe_3O was not directly detected by EPMA, scattered dark areas within the Zr_2Fe primary phase having average $Z=35.3$ could be attributed to Zr_6Fe_3O (average $Z=31.8$).

3.4. Activation study

Initial absorption rates for activated samples were determined from deuterium pressure *vs.* time data that was modeled with the rate equation:

$$\frac{RT}{w}\frac{\mathrm{d}n_{D_2}}{\mathrm{d}t}=\frac{V}{w}\frac{\mathrm{d}P}{\mathrm{d}t}=k_aP \tag{1}$$

which when integrated gives the expression:

$$2.303\log\left(\frac{P}{P_0}\right)=\frac{V}{w}k_at \tag{2}$$

where w is the weight of the sample, n_{D_2} is the number of moles of deuterium, V is the system volume, P and P_0 are the pressure and starting pressure, respectively, and k_a is an absorption rate constant. Thus, a plot of $\log(P/P_0)$ *vs.* time has slope $(V/2.303w)k_a$, and zero intercept. Figure 5 shows $\log(P/P_0)$ *vs.* time for three different sets of activation conditions for the first 2 s. Once k_a is determined by linear regression of the first 2 s of the absorption data, the initial rate (kPa L s^{-1} g^{-1}) is calculated from:

$$\frac{RT}{w}\left(\frac{\mathrm{d}n_{D_2}}{\mathrm{d}t}\right)_{t=0}=k_aP_0 \tag{3}$$

The various activation conditions studied and the resulting initial deuterium absorption rates from the 2^3 factorial experiment are shown in Table 3. With the exception of samples activated at low temperature and

TABLE 3. Test matrix and results for 2^3 factorial getter activation test

Run	Temperature (°C)	Activation time (h)	Vacuum press (Pa)	Rate (kPa l s^{-1} g^{-1})
1	500	4	2.5	0.7468
2	500	4	3×10^{-4}	0.5377
3	500	16	2.5	0.4140
4	500	16	3×10^{-4}	0.7730
5	350	4	2.5	0.0430
6	350	4	3×10^{-4}	0.6028
7	350	16	2.5	0.0017
8	350	16	3×10^{-4}	0.6829

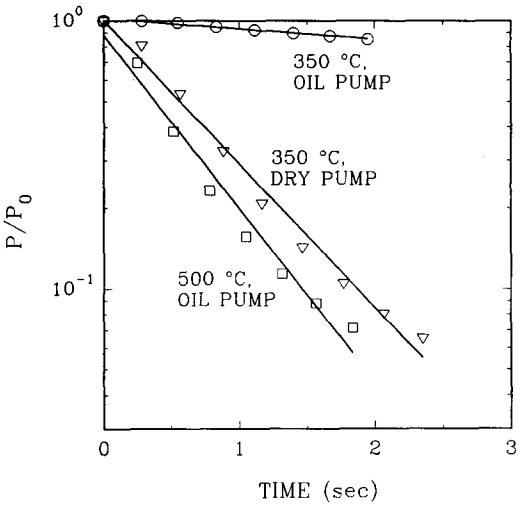

Fig. 5. Log(P/P_0) *vs.* time plots used to determine initial deuterium absorption rate in the 2^3 factorial test.

TABLE 4. Main effect values determined from 23 factorial test

Variable	Main effect
Temperature	0.285
Time	−0.015
Vacuum condition	−0.348

under higher vacuum pressure (oil-sealed rotary vane pump), all initial absorption rates had values between 0.414 and 0.773 kPa L s^{-1} g^{-1}. Samples activated under higher pressure and at low temperature yielded significantly lower initial absorption rates.

The main effects calculated from the statistical test are shown in Table 4. The main effect is a relative number which indicates the relative effect of each variable on the response parameter (initial absorption rate). The larger the main effect, the greater the effect of the variable on the response parameter. Temperature and vacuum conditions have the largest effect on the initial absorption rate, whereas time does not appear to affect the activation process significantly.

3.5. *P–C–T measurements*

Deuterium absorption isotherms for Zr_2Fe at temperatures between 200 and 500 °C are shown in Fig. 6. At approximately 6 kPa L g^{-1}, the slope of the 400 °C isotherm decreases and the isotherm eventually contacts the 350 °C isotherm at approximately 10 kPa L g^{-1}. Similarly, the isotherm at 500 °C undergoes a slope change at about 5 kPa L g^{-1} and nearly contacts the isotherms at 350 and 400 °C. During measurement of the 500 °C isotherm, it was observed that there was initially a rapid reaction of D_2 with the getter that was essentially complete within 10 s. However, this was followed by a slow decrease in system pressure. This observation indicated that initial deuterium reaction and equilibration with the sample was rapid, but that a slow solid-state reaction was occurring that consumed gas phase deuterium. After running the isotherm at 500 °C again (Fig. 7) with longer equilibration time (1 h) it was apparent that at loadings higher than approximately 2 kPa L g^{-1} a reaction that consumed additional deuterium from the gas phase was occurring. At the lower temperatures (⩽350 °C), reaction was complete within 10 s, but the final pressure did not

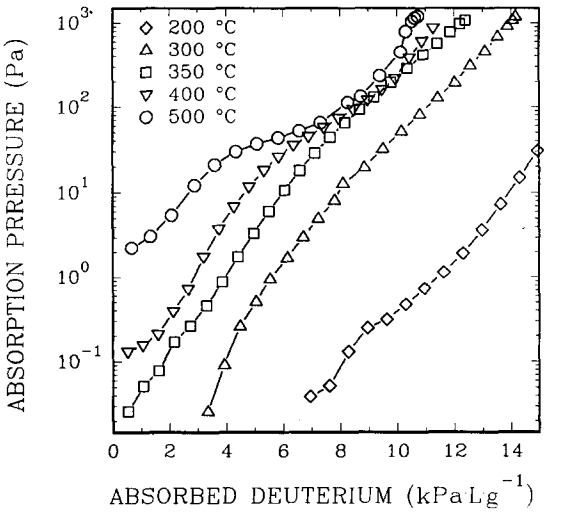

Fig. 6. Deuterium absorption isotherms for SAES St 198.

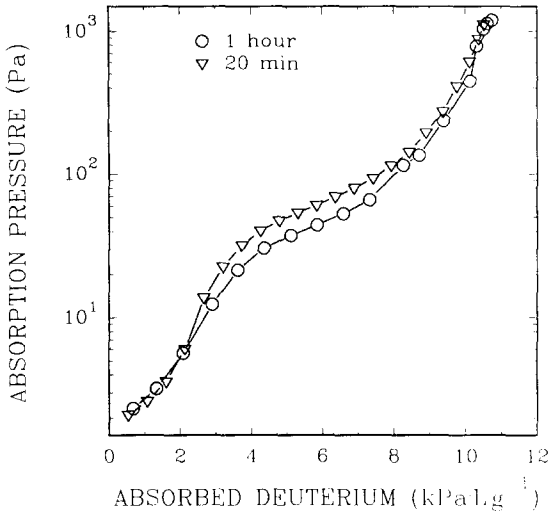

Fig. 7. Deuterium absorption isotherms at 500 °C for equilibration times of 20 min and 1 h for SAES St 198.

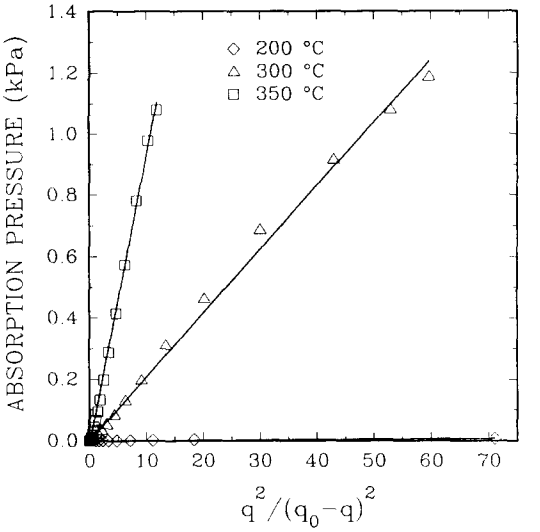

Fig. 8. Absorption pressure *vs.* $q^2/(q^*-q)$ for SAES St 198 at temperatures of 200, 300 and 350 °C.

change. Absorption isotherms at 350 °C run at equilibration times of 20 min and 1 h were identical, indicating that the rate of secondary reaction on the time-scale of the isotherm measurement was insignificant at temperatures of 350 °C and below, and that equilibrium was reached in less than 20 min at temperatures of 350 °C and below.

Further observation of the absorption isotherms in Fig. 6 indicates that there appears to be no α-phase to hydride phase transition. The fact that the isotherms below 350 °C are continuous and show no plateau indicates that deuterium absorption occurs by solution of deuterium atoms into the bulk lattice with no abrupt lattice phase transition. Given this, it is possible to describe the equilibrium thermodynamics with a simple chemical equilibrium expression. The following can be written for the reaction of deuterium gas with lattice deuterium sites:

$$D_2 + 2S \rightleftharpoons 2DS \tag{4}$$

where S is a vacant absorption site. The equilibrium expression for this reaction is:

$$K_{eq} = \frac{[DS]^2}{P_{D_2}[S]^2} \tag{5}$$

where K_{eq} is the equilibrium constant, P_{D_2} is the deuterium partial pressure, and [S] and [DS] are the concentrations of vacant and deuterium-occupied sites in the metal lattice, respectively. This can also be written in terms of the getter loading, q, and the value of q at full loading, q^*:

$$P_{D_2} = \frac{q^2}{K_{eq}(q^*-q)^2} \tag{6}$$

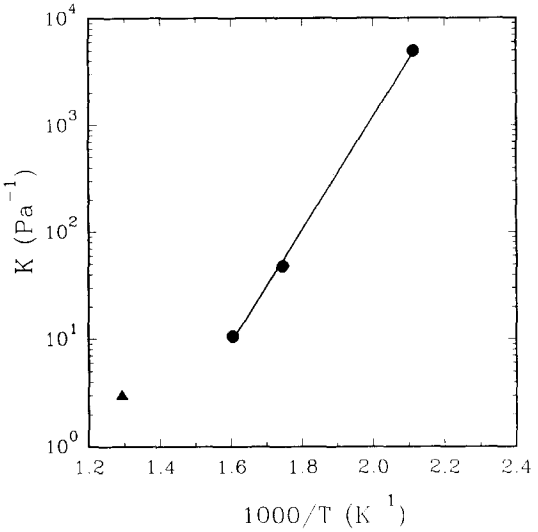

Fig. 9. Van't Hoff plot of the equilibrium constants.

A value of 15.998 kPa L g^{-1} was used for q^*. This value was determined by allowing deuterium to react with a sample, followed by allowing the sample to cool to room temperature. The amount of deuterium absorbed in the sample at room temperature was 15.998 kPa L g^{-1}, and was considered the maximum loading of St 198. A plot of P_{D_2} vs. $q^2/(q^*-q)^2$ would be a straight line with slope $1/K_{eq}$. Figure 8 shows this plot for the *P–C–T* data of Fig. 6 at temperatures of 350 °C and below. At the higher temperatures, due to the slow reaction occurring in the lattice, the data deviated significantly from the model, so these data were excluded from Fig. 8. A van't Hoff plot of the equilibrium constants determined from the slope of the lines in Fig. 8 is shown in Fig. 9. The value of the equilibrium constant at 400 °C is included in Fig. 9, and it is seen that this

point deviates significantly from the data at lower temperatures (200–350 °C). From the slope of this plot, an absorption enthalpy, ΔH_a of 101.8 kJ mol^{-1} is calculated. Thus, the deuterium *P–C–T* data for the full range of loadings and at temperatures of 350 °C and below are described by:

$$K_0 e^{-(\Delta H_a/RT)} = \frac{q^2}{P_{D_2}(q^* - q)^2} \quad (7)$$

where K_0 was determined from the intercept of Fig. 9 to be 3.24×10^{-8} Pa^{-1}.

3.6. X-Ray diffraction analysis of deuterium-loaded samples

Samples loaded with deuterium during the absorption isotherm measurements were analyzed by X-ray diffraction to probe changes that occurred from reaction with deuterium. Table 5 shows relative intensities of the strongest X-ray diffraction peaks for several phases in deuterium-loaded samples as a function of temperature. Figure 10 shows diffraction patterns for as-received samples and samples loaded with deuterium at 200 and 500 °C. While Zr_2Fe, $ZrFe_2$, α-Zr and Zr_6Fe_3O are the dominant phases in the as-received material (detected by XRD), the addition of deuterium at 200 °C causes the Zr_2Fe, α-Zr and Zr_6Fe_3O peaks to disappear. Disappearance of the Zr_2Fe peak is explained by formation of Zr_2FeD_x, as indicated by the Zr_2FeD_x peaks at 200 °C. Alpha-zirconium probably forms ZrD_2, but the absence of ZrD_2 peaks is surprising, and may be due to very small ZrD_2 domains that are not detectable by XRD. Zr_6Fe_3O which was detected in the as-received material was no longer present in samples exposed to temperatures of 350 °C or less. Disappearance of this phase may come about upon activation, during which oxygen in high concentration regions (surface or oxide phase regions) diffuses into the bulk lattice.

ZrD_2 peaks are absent in the as-received and 200 °C samples, but appear in samples loaded with deuterium at 300 and 350 °C, and become the most intense peaks in the diffraction patterns at 400 and 500 °C. The

TABLE 5. Relative intensities of the strongest X-ray diffraction peaks for as-received and deuterium-exposed SAES St 198

Absorption temperature (°C)	Phase					
	Zr_2Fe	$ZrFe_2$	α-Zr	Zr_6Fe_3O	Zr_2FeD_x	$ZrD_{1.8}$
as-received	100	76	49	53	0	0
200	0	23	0	0	100	0
300	0	24	0	0	100	24
350	0	34	0	0	100	21
400	0	55	0	38	29	100
500	0	57	0	35	0	100

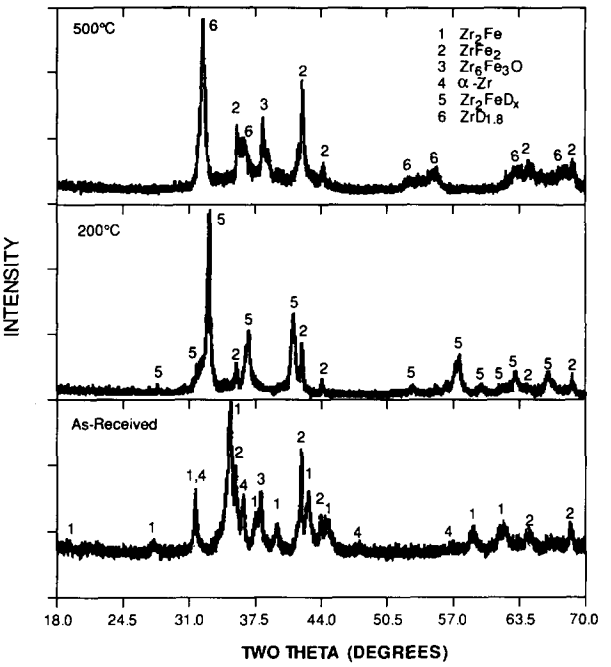

Fig. 10. X-ray powder diffraction patterns of SAES St 198 samples after conducting absorption isotherms at 200 and 500 °C.

Zr_2FeD_x peak becomes less intense at 400 °C, and is absent at 500 °C. Thus, on the time-scale of our experiments, Zr_2FeD_x is stable at temperatures of 350 °C and below. Above 350 °C, decomposition of Zr_2FeD_x occurs rapidly. The reason for the reappearance of Zr_6Fe_3O peaks at 400 and 500 °C is unclear. Observation of the diffraction patterns, as well as the data in Table 5 does not give clear indication of an increase in the intensity of the $ZrFe_2$ peaks, but it appears that there may be an increase in the $ZrFe_2$ peak intensity at higher temperatures.

4. Discussion

Detection of primary Zr_2Fe by SEM and XRD is consistent with the elemental analysis and the Zr–Fe binary phase diagram [12]. The phase diagram indicates that elemental zirconium should be the secondary phase in the eutectic. However, EPMA indicates that this secondary phase is Zr_5FeSn, so tin appears to play a role in the eutectic behavior of Zr_2Fe. No Zr_5FeSn XRD peaks were detected, but this may be due to the small quantity of this phase which may be below the detection limit of XRD. The cubic phase identified as Zr_6Fe_3O likely results from oxygen contamination of Zr_2Fe. The iron–zirconium phase diagram indicates that at temperatures less than 775 °C, Zr_2Fe is unstable and will undergo a transformation to Zr_3Fe and $ZrFe_2$. Evidently the kinetics of this transformation is slow since no Zr_3Fe was detected in any of our samples.

The absence of Zr_3Fe in our samples is surprising, since it is often detected in cast and annealed binary zirconium–iron alloys with compositions similar to St 198 [13].

Results from the activation study indicate that at the lower activation temperature (350 °C) and under poor vacuum conditions, initial deuterium absorption rates at 350 °C were significantly lower. At higher activation temperature (500 °C) deuterium absorption rate at 350 °C is not influenced by vacuum conditions, and is rapid for both poor and good vacuum quality. Most likely, the higher gas phase oxygen, water and other impurity concentrations under poor vacuum conditions cannot be adsorbed, decomposed and diffused into the bulk at a sufficiently fast rate to maintain a clean and active getter surface. At the higher temperature, adsorption, decomposition and diffusion of impurities onto the bulk is rapid, and there is little accumulation of these impurities on the surface. Previous investigations [9–11] have determined that diffusion of oxygen and carbon into the bulk alloy occurs at typical getter operating conditions. Reduction of surface metal oxides is more rapid and complete at higher temperatures [11]. It is also possible that cracking of the surface oxide layer plays a role in the getter activation. The main effect value for the influence of activation time on the activation process (Table 4) indicates that time has a very small effect on the St 198 activation process.

While measuring absorption isotherms at 400 and 500 °C, it became apparent that a slow reaction which consumed deuterium might be occurring in the lattice (Fig. 9). The XRD results presented in Table 5 and in Fig. 10 indicate that on the time-scale over which our samples were exposed, decomposition of Zr_2FeD_x begins to occur rapidly above 350 °C. While it is clear that this decomposition proceeds with formation of ZrD_2, the state of the remaining iron is not certain. Some iron may be consumed in the formation of $ZrFe_2$ as indicated in Table 5. Previous investigators have indicated that Zr_2FeH_x proceeds with the formation of ZrH_2 and $ZrFe_2$. Van Essen and Buschow [6] indicate that for 4 h at 50 °C and under hydrogen pressure of 4.05 MPa, reaction of hydrogen with Zr_2Fe forms ZrH_2 and $ZrFe_2$. Although these authors indicate that results from X-ray diffraction led to this conclusion, the details of their X-ray diffraction were not provided, so it is uncertain from the paper which of the decomposition products (ZrH_2 or $ZrFe_2$) was detected. It is surprising that the decomposition products were detected at such a low temperature, however, the extremely high hydrogen pressure used may be the cause for this. Aubertin *et al.* [7] also report formation of ZrH_2 and $ZrFe_2$ based on XRD analysis of samples, but their samples were exposed to temperatures of 850 °C, where migration of atoms is sufficiently fast to allow formation of significant quantities of additional phases, such as ZrH_2 and $ZrFe_2$. Manini *et al.* [4] examined the phases present in Zr_2Fe samples fully and partially loaded with hydrogen. XRD analysis of their partially loaded samples suggest some formation of $ZrFe_2$, whereas $ZrFe_2$ peaks in diffraction patterns of the fully loaded samples were distinct. Their samples were held at 500 °C for 2 h.

Observation of the XRD results in Table 5 and in Fig. 12 indicates that while it is clear that ZrD_2 is forming at the higher temperatures, formation of $ZrFe_2$ at the higher temperatures (>350 °C) is not obvious. Our samples were exposed to deuterium for about 8 h, which is significantly longer than the samples examined by Manini *et al.* However, the deuterium loading of our samples was not constant, so a straightforward comparison between our samples and those of Manini *et al.* is not possible. The 500 °C absorption isotherms in Fig. 7 which were collected for equilibration times of 20 min and 1 h indicate, however, that at low loading (<2 kPa L g) there is little difference between the two isotherms, but as loading increases the decomposition reaction is more rapid. It thus appears that the decomposition reaction rate increases with deuterium loading. It is likely that fully loaded Zr_2Fe samples examined by Manini *et al.* [4] and Aubertin *et al.* [7] experienced significantly higher decomposition rates due to their full loading.

Our samples are probably similar to the partially loaded samples of Manini *et al.* which showed minor formation of $ZrFe_2$. The reaction of deuterium with Zr_2Fe and subsequent decomposition of Zr_2FeD_x to ZrD_2 and $ZrFe_2$ can be described as follows:

$$Zr_2Fe + \frac{x}{2} D_2 \underset{\text{fast}}{\rightleftharpoons} Zr_2FeD_x \xrightarrow[\text{depending on T}]{\text{slow or fast}}$$

$$\frac{x}{2} ZrD_2 + \frac{x}{6} ZrFe_2 + \left(1 - \frac{1}{3}x\right) Zr_2Fe \quad (8)$$

where $0<x<3$. The first step is fast, while the second step is slow at low temperatures, and becomes faster at higher temperature. Zr_2Fe formed in eqn. (8) subsequently reacts with deuterium from the gas phase to restore the equilibrium concentration of Zr_2FeD_x:

$$Zr_2Fe + \frac{x}{2} D_2 \rightleftharpoons Zr_2FeD_x \quad (9)$$

and this explains the observed slow deuterium consumption from the gas phase. Equation (8) predicts stoichiometric formation of $ZrFe_2$. However, the data in Table 5 indicates that while formation of ZrD_2 is distinct, there is only a slight indication of $ZrFe_2$ formation, so eqn. (8) cannot fully explain the behavior. It is also possible that Zr_2FeD_x could decompose to ZrD_2 without forming $ZrFe_2$. For example:

$$Zr_2FeD_x + \left(2 - \frac{1}{2}x\right)D_2 \longrightarrow 2ZrD_2 + Fe \qquad (10)$$

which would proceed with formation of Fe as well as ZrD_2. Our XRD results do not detect metallic iron, although iron produced in this reaction might not crystallize to sufficiently large crystals to be detected by XRD. Similar high temperature disproportionation reactions have been observed with other intermetallic compounds, where the element having high hydrogen affinity reacts to form a stable metal hydride. It is possible that both eqns. (8) and (10) are occurring.

Decomposition of Zr_2Fe can be expected in applications involving high temperature and significant hydrogen isotope loading. For applications such as tritium removal from glovebox atmospheres or process gas streams, extended exposure of the material to high temperature (350 °C) will be the case, but very low tritium loadings are expected. The data presented in Fig. 7 indicate that decomposition of Zr_2Fe at loadings less than about 2 kPa L g^{-1} is slow even at 500 °C.

Although previous investigators have indicated that tritium recovery and regeneration of St 198 capacity can be achieved by heating the alloy to 700 °C under vacuum or under noble gas purge [2], we believe that an investigation is needed to fully characterize this process. Heating tritium-loaded St 198 to high temperature will likely cause the reaction of some tritium to form ZrT_2. While some tritium will be recovered, it is likely that a portion of the tritium will be converted irreversibly to ZrT_2. Furthermore, the regenerated material would show a decreased capacity for gettering tritium, and possibly other material differences from the freshly activated St 198. Further investigation is necessary to establish the optimum regeneration conditions.

It was shown above that the *P–C–T* data can be correlated with a simple equilibrium expression (eqn. (7)). While previous investigators have used a different expression to correlate *P–C–T* data for Zr_2Fe [4, 5], eqn. (7) represents an improvement to the previous expressions since it applies to the full range of deuterium loadings. Due to secondary reactions occurring in the lattice at temperatures above 350 °C, it is not possible to provide a reliable correlation at temperatures above 350 °C.

Analysis of the *P–C–T* data resulted in an absorption enthalpy (ΔH_a) of 101.8 kJ mol^{-1} D_2. Other investigators have measured ΔH_a values for other zirconium alloy getters. ΔH_a for deuterium absorption in St 101 is reported to be 138.2 kJ mol^{-1} D_2 [14, 15], and ΔH_a for St 707 is 120.6 kJ mol^{-1} D_2 [14]. St 101 has much lower absorption pressures than St 198, and it thus should have a higher absorption enthalpy. The absorption pressures of St 198 are similar to those of St 707, so a similar absorption enthalpy is expected, but the value for St 198 that we report is lower than that of Boffito *et al.* [14]. However, the absorption enthalpy reported by Boffito *et al.* was determined from *P–C–T* data for low deuterium loading in the alloy. Our absorption enthalpy result for St 198 was extracted from *P–C–T* data covering the full deuterium capacity of the alloy. Due to repulsive interaction effects between deuterons in the metal lattice, the absorption enthalpy is most likely a function of the alloy deuterium loading. Repulsive interactions would likely cause lower absorption enthalpy at higher deuterium loading, and this may be the reason for our lower absorption enthalpy value.

5. Conclusion

St 198 consists mostly of the Zr_2Fe phase with multiphases of $ZrFe_2$, Zr_5FeSn, α-Zr and Zr_6Fe_3O. The material becomes well activated when evacuated at temperatures higher than 350 °C for 4 h or longer, as long as a relatively high vacuum is maintained. Higher activation temperatures should be considered for systems with poorer vacuum quality. Deuterium *P–C–T* data for the full range of getter deuterium loadings and at temperatures of 350 °C or lower can be correlated using a simple equilibrium expression. At temperatures higher than 350 °C, Zr_2FeD_x decomposes at a significant rate to ZrD_2, and possibly $ZrFe_2$ and Fe. However, for applications involving very low hydrogen isotope loading, such as stripping low tritium concentrations from glovebox or process atmospheres, the decomposition reaction probably would be insignificant. Recovery of tritium absorbed on St 198 by heating under vacuum at temperatures higher than 500 °C would likely cause decomposition of Zr_2FeT_x with the formation of irreversible ZrT_2, and a decreased capacity of the regenerated material. An investigation is necessary to establish the feasibility and optimum conditions for recovering hydrogen isotopes from St 198.

Acknowledgments

The authors wish to thank many individuals for contributions to this work. Mercury porosimetry was performed by R.A. Malstrom, bulk elemental analyses by ICP–MS and XRF were provided by C.J. Coleman and A.R. Jurgensen, respectively. F.E. Odum and A.S. Holston prepared the samples for SEM and EPMA. SEM examination was performed by A.S. Holston and J.E. Durden. EPMA was performed by L.F. Tovo and S.F. McDaniel. A.R. Jurgensen and R.E. Howell provided the XRD analyses. W.L. Moyer assisted with the

activation study and *P–C–T* measurements. This work was performed under the auspices of the Department of Energy under contracts DE-AC09-89SR18035 and W-7405-ENG-36.

References

1 N.P. Kherani, W.T. Shmayda and R.A. Jalbert, *Proc. 12th Symp. on Fusion Eng., Monterey, CA, October 12–16, 1987*, I.E. Conf. No. 11702.
2 W.T. Shmayda, N.P. Kherani, B. Wallace and F. Mazza, *Fusion Technol., 21* (1992) 616.
3 A. Nobile, Jr., Experience using metal hydrides for tritium processing, *Fusion Technol., 20* (2) (1991) 186.
4 P. Manini, C. Boffito, G. Gasparini, C. Maran and A. Gallitognotta, *Proc. 2nd European Vacuum Conf., Trieste, 1990.*
5 C. Boffito, F. Doni and L. Rosai, *J. Less-Common Met., 104* (1984) 149.
6 R.M. Van Essen and K.H.J. Buschow, *J. Less-Common Met., 64* (1979) 277.
7 F. Aubertin, U. Gonser and S.J. Campbell, *J. Less-Common Met., 101* (1984) 437.
8 Powder Diffraction Files, JCPDS–International Center for Diffraction Data.
9 K. Watanabe, K. Ichimura, K. Ashida, M. Matsuyama and T. Takeuchi, *Fusion Technol., 14* (1988) 729.
10 K. Ichimura, M. Matsuyama and K. Watanabe, *J. Vac. Sci. Technol. A, 5* (2) (1987) 220.
11 M. Sancrotti, G. Trezzi and P. Manini, *J. Vac. Sci. Technol., A 9* (2) (1991) 182.
12 T.B. Massalski (Editor-in-Chief), *Binary Alloy Phase Diagrams*, Vol. 3, ASM International, 2nd edn., 1990, p. 1798.
13 T.O. Malakhova and Z.M. Alekseyeva, *J. Less-Common Met., 81* (1981) 293.
14 C. Boffito, B. Ferrario and D. Martelli, *J. Vac. Sci. Technol., A 1* (2) (1983) 1279.
15 R.J. Knize, *J. Vac. Sci. Technol., 20* (1982) 1135.